Lawrence Berkeley National Laboratory

Title
Directed Assembly of Cuprous Oxide Nanocatalyst for CO2 Reduction Coupled to Heterobinuclear ZrOCoII Light Absorber in Mesoporous Silica

Permalink
https://escholarship.org/uc/item/53p8m0gz

Authors
Kim, Wooyul
Frei, Heinz

Directed Assembly of Cuprous Oxide Nanocatalyst for CO$_2$ Reduction Coupled to Heterobinuclear ZrOCo^{II} Light Absorber in Mesoporous Silica

Wooyul Kim and Heinz Frei*

Physical Biosciences Division, Lawrence Berkeley National Laboratory, University of California, Berkeley, California 94720, United States

S *Supporting Information*

ABSTRACT: Hierarchical assembly of an oxo-bridged binuclear ZrOCo^{II} light absorber unit coupled to a cuprous oxide nanocluster catalyst for CO$_2$ reduction on mesoporous silica support is demonstrated. The proper positioning of the Cu oxide cluster was achieved by photodeposition of a [Cu(NCCH$_3$)$_4$]$^{2+}$ precursor by visible light excitation of the ZrOCo charge transfer chromophore, followed by mild calcination at 350 C. Illumination of the Cu$_x$O$_y$-ZrOCo unit so formed in the presence of a diethylamine electron donor resulted in the reduction of surface Cu centers to Cu^0 as demonstrated by the characteristic infrared band of adsorbed ^{13}CO probe molecules at 2056 cm^{-1}. For analogous Cu$_x$O$_y$-TiOCo^{II} units, the oxidation state makeup of the surface Cu centers was dominated by Cu^I, and the Cu^0, Cu^I, and Cu^{II} composition was found to depend on the wavelength of MMCT excitation. The observed strong dependence of the CO$_2$ photoreduction yield on the oxidation state of the surface Cu centers directly proves that CO$_2$ is reduced on the Cu$_x$O$_y$ surface, thus establishing that the ZrOCo^{II} unit functions as light absorber, donating electrons to the Cu$_x$O$_y$ catalyst on whose surface CO$_2$ is reduced.

KEYWORDS: photodeposition, carbon dioxide reduction, artificial photosynthesis, photocatalysis, copper oxide catalyst, heterobinuclear light absorber
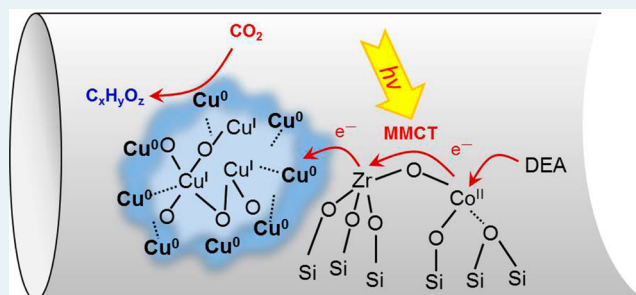
1. INTRODUCTION

Efficient coupling of light absorber and multielectron catalysts for carbon dioxide reduction or water oxidation is a critical, and currently among the most challenging, task for developing viable artificial photosystems for renewable fuel generation. For visible light driven CO$_2$ reduction, typical examples of molecularly defined light absorber-catalyst assemblies are organo Ru or metallo-porphyrin complexes coupled via hydrocarbon linkage or amide bridge to a Re bipyridine tricarbonyl catalyst.[1−4] Exploring an alternative to organometallic systems because of the durability challenge of soft matter, we are pursuing an all-inorganic materials approach using oxo-bridged heterobinuclear units as molecularly defined light absorbers anchored on silica nanoparticle surfaces.[5] Recent demonstration of a heterobinuclear ZrOCo^{II} light absorber coupled to an Ir oxide nanocluster catalyst on mesoporous silica support for the direct photoconversion of CO$_2$ by H$_2$O to CO and O$_2$ was made possible by a photodeposition method that allowed the coupling of the Co donor center to the IrO$_x$ catalyst.[5] The construct affords remarkably efficient charge transfer from the Co center of the Zr^{IV}OCo^{II}→ Zr^{III}OCo^{III} excited charge-transfer unit to the IrO$_x$ cluster, thereby driving the multistep oxidation of H$_2$O to O$_2$. By analogy, this photodepositon method might offer a synthetic

route for coupling a nanocluster catalyst for CO$_2$ reduction to the Zr acceptor center with the goal of photoreducing CO$_2$ beyond two-electron transfer products to four, six, or more highly reduced liquid products such as low alcohols.

Because of their robustness, catalysts in the form of inorganic particles are of special interest. Electrochemical CO$_2$ reduction at metallic Cu electrodes is known to produce a series of more deeply reduced C$_1$ (mainly methane or methanol) and C$_{\geq 2}$ hydrocarbon products.[6−8] Rapidly growing research activity in this area has led to a series of reports regarding factors that influence product distribution or lowering of the (still high) overpotential, specifically surface morphology, nanostructure, oxidation/reduction pretreatment, and oxidation state of surface Cu centers.[9−16] As a consequence, the activity and selectivity of CO$_2$ reduction have markedly improved over the past several years. Particularly promising and relevant to our approach are Cu oxide based particles as multielectron catalysts. Cuprous oxide clusters either deposited on photocatalytic particles or as stand-alone photocatalysts have been reported to afford reduction of CO$_2$ to formaldehyde and even

methanol.[17,18] While barely explored in light driven assemblies, such cuprous oxide nanoclusters hold promise for lowering overpotentials for CO_2 activation and extending the degree of multielectron reduction.

In this work, we demonstrate photodeposition of 3 nm sized cuprous oxide nanoclusters (abbrev. Cu_xO_y) adjacent to binuclear units $ZrOCo^{II}$ or $TiOCo^{II}$ anchored on the silica pore surfaces of SBA-15. The oxidation state of surface Cu, determined by the infrared mode of adsorbed CO, can be controlled by reduction of the Cu_xO_y cluster upon metal-to-metal charge-transfer state (MMCT) of the binuclear light absorber. The observed strong dependence of the yield of CO_2 photoreduction on the oxidation state of surface Cu confirms that the heterobinuclear unit functions as a light absorber, donating electrons to the Cu_xO_y catalyst on whose surface catalytic CO_2 reduction takes place.

2. EXPERIMENTAL SECTION

2.1. Materials and Chemicals. Reagents used were zirconocene dichloride ($[ZrCp_2Cl_2]$, > 99%, Strem), titanocene dichloride ($[TiCp_2Cl_2]$, > 97%, Aldrich), anhydrous cobalt chloride (>98%, Fluka), triethylamine (TEA, > 99%, Aldrich), diethylamine (DEA, > 99.5%, Aldrich), acetonitrile (>99.9%, Honeywell), ^{13}C-carbon dioxide (99% ^{13}C, Cambridge Isotope lab, Inc.), ^{13}C-carbon monoxide (99%, Aldrich), Pluronic P-123 (Aldrich), concentrated hydrochloric acid (37%, Aldrich), and tetrakis acetonitrile copper(I) hexafluorophosphate $[Cu^I(NCCH_3)_4]PF_6$. Solvents were dehydrated with 3 Å molecular sieves for acetonitrile, TEA, and DEA and 4 Å molecular sieves (Linde) for anhydrous methylene chloride for at least 72 h. Approximately 5 g of molecular sieves activated at 170 °C under a vacuum for 24 h were used per 100 mL of solvent. Acetonitrile, TEA, and DEA liquids were purged with nitrogen for 1 h and stored in a N_2 glovebox before use. Anhydrous cobalt chloride was heated at 120 °C under a vacuum for 16 h before use in order to obtain an air-free sample. DEA for CO_2 reduction experiments was placed in a Schlenk flask and frozen in liquid nitrogen, evacuated, and allowed to thaw. This process was repeated three times to completely degas DEA. $[Cu^I(NCCH_3)_4]PF_6$, $[ZrCp_2Cl_2]$, and $[TiCp_2Cl_2]$ were kept in a N_2 glovebox to avoid water contamination.

2.2. Synthesis of ZrOCo SBA-15 and TiOCo SBA-15. Mesoporous silica SBA-15 was synthesized according to the method used in previous reports.[19,20] Both binuclear ZrOCo and TiOCo units were assembled in the pores of SBA-15 by reaction of the tetrahedral complex $[Co^{II}(NCCH_3)_2Cl_2]$ on the nanopore surface of Zr-SBA-15 and Ti-SBA-15, respectively.[5,21-23] Briefly, Zr or Ti acceptor metal is first covalently attached to the silanol surface using a metallocene precursor (zirconocene dichloride or titanocene dichloride) in the presence of triethylamine, whose function is to partially deprotonate surface silanol groups.[19-26] Stirring at room temperature in a dry N_2 box yields the as-synthesized tripodally anchored single metal with cyclopentadienyl ligand, which is readily removed by calcination in the air to yield the isolated tetrahedral Ti or Zr center. To yield the oxo-bridged binuclear unit, covalent anchoring of Co as a second metal was conducted with $[Co^{II}(NCCH_3)_2Cl_2]$ as a precursor and triethylamine in acetonitrile as reported previously.[5,21-23] The reaction proceeds selectively due to the enhanced reactivity of the TiOH and ZrOH groups compared to the surrounding surface silanol groups, which are much more abundant, by

virtue of the greater acidity of the TiOH and ZrOH groups.[27] Following each grafting step (Zr (or Ti), Co), calcination was conducted to remove the remaining organic ligand at 550 °C for 12 h (Zr, Ti) and 350 °C for 5 h (Co), respectively. The detailed synthetic method and characterization of $ZrOCo^{II}$–SBA-15 including comprehensive spectroscopic characterization by powder X-ray diffraction (PXRD), extended X-ray absorption fine structure (EXAFS), FT-IR, FT-Raman, optical spectroscopy, and ICP analysis were described in detail in our previous papers.[5,21-23] Specifically, ICP analysis gave 1.0 ± 0.1 mol % Zr and 0.7 ± 0.1 mol % Co, which is within uncertainties close to the values obtained for the previously published ZrCo SBA-15 samples.[23] Because the intensity of the MMCT absorption measured by DRS normalized to wafer thickness was also close to the MMCT intensity of the previously synthesized samples,[23] we conclude that the ratio of binuclear ZrOCo units to isolated Zr or Co centers is the same within uncertainty as for the previous sample. In that case, curve fitting analysis of EXAFS measurements of the Zr and Co K-edge showed that the majority (at least 80%) of all Zr centers form a binuclear unit with Co, while all Co centers are bound to Zr.[23]

2.3. Photochemical Deposition of Cu_xO_y-$ZrOCo^{II}$SBA-15 and Cu_xO_y-$TiOCo^{II}$SBA-15. The precursor $[Cu^I(NCCH_3)_4PF_6]$ for the assembly of copper oxide nanoclusters (abbrev. Cu_xO_y) was loaded into SBA-15 pores by adding 100 mg of as-synthesized $ZrOCo^{II}$SBA-15 or $TiOCo^{II}$SBA-15 to 1 mM (19 mg) of $[Cu^I(NCCH_3)_4]PF_6$ dissolved in dichloromethane (50 mL; as-synthesized means that the final calcination step of the $ZrOCo^{II}$ SBA-15 sample was omitted in order to utilize the remaining triethylamine as an electron donor for the Cu photodeposition reaction described below;[23] some experiments were conducted with calcined $ZrOCo^{II}$ SBA-15 subsequently loaded again with triethylamine, which led to identical photodeposition results). The solution was stirred for 3 h at room temperature in a dark environment inside a N_2 glovebox. The powder was filtered, washed two times with 50 mL of dichloromethane, and dried in a vacuum for 8 h. The as-synthesized powder (5 mg) was pressed with a KBr press (13 mm diameter) under ≤1 ton of pressure for 5 s, which was exposed to air (10 h) for oxidizing the Cu complex to $[Cu^{II}(NCCH_3)_4]^{2+}$ and characterized by in situ FT-IR and UV-DRS. The wafer was subsequently evacuated for 1 h in a homemade stainless steel optical cell equipped with a quartz window. The wafer containing $[Cu^{II}(NCCH_3)_4]^{2+}$ was irradiated at room temperature for 30 min using the 355 nm emission (100 mW cm^{-2}) of a pulsed Nd:YAG laser at 10 Hz (Continuum model Surelite III) or the 458 nm emission (190 mW cm^{-2}) of an Ar ion laser (Coherent model Innova 90C) with the beam expanded to 1 in. diameter. The sample was subsequently calcined at 350 °C for 5 h under a flow of air, resulting in the formation of a greenish pellet containing $ZrOCo^{II}$ or $TiOCo^{II}$ groups and Cu oxide nanoclusters, termed Cu_xO_y-$ZrOCo^{II}$SBA-15 or Cu_xO_y-$TiOCo^{II}$SBA-15. Typical Cu_xO_y loading was estimated to be 3−4 wt % (Cu/Si ratio) based on ICP measurement, which was in agreement with the analysis of the Cu precursor that remained in solution. The photodeposition of $[Cu^{II}(NCCH_3)_4]^{2+}$ was monitored in situ by UV diffuse reflectance spectroscopy (UV-DRS, Shimadzu model UV-2450 spectrometer equipped with an integrating sphere model ISR-2200), in situ FT-IR spectroscopy (Bruker model IFS66 V equipped with LN$_2$ cooled MCT detector Kolmar model KMPV8-1-J2 with an 8 μm band gap), and a UV-Raman spectroscopy system. The

Raman spectrometer was used with a continuous wave intracavity-doubled Ar ion laser (Spectra Physics) operating at 244 nm. Scattered light was collected and directed into a fully automated spectrometer (iHR550, Horiba) after passing through bandpass and edge filters. Spectra were recorded with an open electrode CCD detector (SynapseHoriba, 1024 × 256 pixels). Transmission electron microscopic imaging was conducted with a CM300 instrument, and EDX data were collected on a TitanX instrument of the National Center for Electron Microscopy.

2.4. Photochemical Reduction of Cu_xO_y-ZrOCo^{II}SBA-15 and Cu_xO_y-TiOCo^{II}SBA-15. The calcined wafer was placed in a home-built stainless infrared vacuum cell equipped with CaF_2 windows and mounted in the FT-IR spectrometer. After 3 h of evacuation at room temperature, 0.5 Torr of diethylamine was admitted to the infrared cell. For photoreduction of the Cu oxide nanocluster after calcination, the wafer was reloaded with DEA and irradiated at room temperature using the 355 nm emission (100 mW cm^{-2}) for 3 h or 458 nm emission (190 mW cm^{-2}) for 5 h with the beam expanded to the size of the wafer (1 cm diameter).

2.5. Photochemical CO_2 Reduction. The reduced (or nonreduced) Cu_xO_y-ZrOCo^{II} SBA-15 and Cu_xO_y-TiOCo^{II}SBA-15 wafer (5 mg) was placed in a home-built stainless infrared vacuum cell (volume 3.7 cm^3) equipped with CaF_2 windows and mounted in the FT-IR spectrometer for in situ monitoring of photocatalysis. After evacuation for 3 h at room temperature, diethylamine (0.5 Torr) and $^{13}CO_2$ (760 Torr) gas were admitted to the infrared cell. After a 30 min dark period to confirm that no spectral changes occurred in the absence of light, laser photolysis (355 nm, 100 mW cm^{-2}) was conducted at room temperature over a period of 5 h and infrared spectra recorded at regular intervals. The spectral resolution was 0.25 cm^{-1}. To identify the origin of any carbon containing product, all experiments were carried out using isotopically labeled $^{13}CO_2$. Gas phase ^{12}CO and ^{13}CO can readily be differentiated by the characteristic ro-vibrational bands in the 2200−2000 cm^{-1} region.

3. RESULTS

3.1. Photodeposition of Cu_xO_y Coupled to Binuclear Light Absorber Unit. Our approach for assembling a Cu oxide nanocluster coupled to the Zr center of the ZrOCo unit is based on recent precedents for the coupling Ti or Ir precursors to other metal centers anchored on a silica nanopore surface through redox reactions. For example, we have shown that a Ti^{III} precursor undergoes spontaneous redox coupling with Cr^{VI} centers anchored on mesoporous silica surfaces to form Ti^{IV}OCr^V units.[22] Similarly, the dark redox reaction of an Ir^{III} precursor with anchored Cr^{VI} centers was found to form CrOIr^{IV} units. Subsequent calcination at mild temperature gave an IrO$_2$ nanocluster coupled to the Cr center.[28] Reaction of an Ir^{III} precursor with the Ti^{IV}OCr^V unit mentioned above followed by calcination yielded a TiOCr^{III} group coupled to an IrO$_2$ catalyst cluster.[29] By analogy, Ir oxide clusters coupled to Co centers of ZrOCo units were made by a photoinduced version of this chemistry, namely excitation of ZrOCo centers to generated transient Co^{III} that couples with an Ir^{III} precursor, followed by calcination to obtain an Ir oxide nanocluster coupled to Co.[5] Building on these precedents, we proposed here that assembly of a Cu oxide nanocluster coupled to the Zr center of a ZrOCo unit should be feasible by generating transient Zr^{III} upon photoexcitation of Zr^{IV}OCo^{II} in the

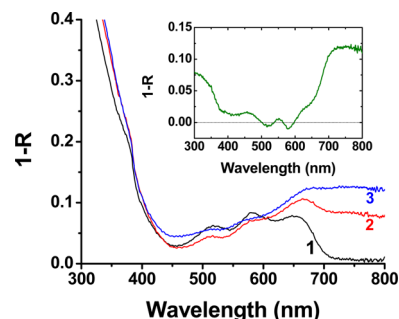presence a reducible Cu^{II} precursor, followed by mild calcination. Figure 1 shows the optical spectra of ZrO-

Figure 1. UV−vis DRS of ZrOCo^{II}SBA-15 after loading of [Cu^I(NCCH$_3$)$_4$]$^+$ (trace 1, black) under a N$_2$ atmosphere and after exposing the sample to air for 1 h (trace 2, red) and 10 h (trace 3, blue). Inset: Difference spectrum trace (3 − 1). The sample wafer (5 mg, loaded with 0.8 mg [Cu^I(NCCH$_3$)$_4$]PF$_6$) was held in a vacuum.

Co^{II}SBA-15 after loading of the [Cu^I(NCCH$_3$)$_4$]$^+$ complex (trace 1, black). In order to oxidize the Cu^I complex to Cu^{II}, the sample was exposed to air for 1 h (trace 2, red) and a total of 10 h (trace 3, blue). As we reported previously, loading of the [Cu^I(NCCH$_3$)$_4$]$^+$ complex into mesoporous silica and evacuation of the sample at room temperature results in Cu^I centers in the silica nanopores that remain coordinated with acetonitrile ligands.[20] Growth of the very broad Cu^{II} d−d band ($^2E \rightarrow {^2T_2}$ transition) with a maximum close to 800 nm is observed, indicating a distorted octahedral coordination of the Cu^{II} center.[30−33] The difference spectrum (Figure 1 inset) shows the emerging Cu^{II} band most clearly, although the profile is perturbed by the ligand field bands of Co^{II}. The oxidation of the Cu center is further confirmed by comparison of the in situ FT-IR spectra in the ν(C≡N) region of the CH$_3$CN ligands attached to anchored Cu^I (2331 and 2302 cm^{-1})[19] and Cu^{II}, which are red-shifted to 2322 and 2296 cm^{-1}, as shown in Figure 2.
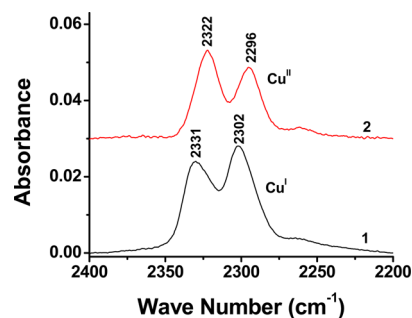

Figure 2. FT-IR spectra of ZrOCo^{II}SBA-15 upon loading of [Cu^I(NCCH$_3$)$_4$]$^+$ (trace 1, black) and after exposing to air for 10 h (trace 2, red). The sample (5 mg wafer loaded with 0.8 mg [Cu^I(NCCH$_3$)$_4$]PF$_6$) was held under a vacuum.

Illumination of the Zr^{IV}OCo^{II} → Zr^{III}OCo^{III} MMCT absorption of this Cu^{II} loaded ZrOCo SBA-15 material at 355 nm (100 mW cm^{-2}) resulted in the photodeposition of the Cu centers under reduction to Cu^I. As can be seen from UV−vis DRS traces in Figure 3a recorded before (trace 1, black) and after 1 h illumination (trace 2, red), the Cu^{II} d−d absorption around 800 nm and the Cu^{II} charge transfer transition decrease under a concurrent rise of the 3d^{10} → 3d^{9}4s^1 absorption of Cu^I

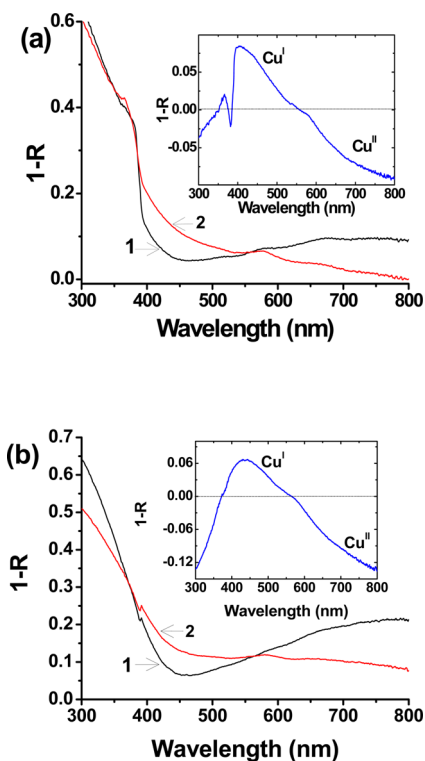**Figure 3.** (a) UV−vis DRS of ZrOCo^{II}SBA-15 loaded with [Cu^I(NCCH$_3$)$_4$]$^+$ after air oxidation for conversion to Cu^{II} (trace 1, black), followed by 1 h of photodeposition at 355 nm (100 mW cm^{-2}; trace 2, red). Inset: Difference spectrum (2 − 1). Sample wafer was 5 mg; [Cu^I(NCCH$_3$)$_4$PF$_6$] loading, 0.8 mg. (b) Same experiment with TiOCo^{II} SBA-15 showing the spectrum before (trace 1, black) and after (trace 2, red) photodeposition at 458 nm irradiation for 1 h (190 mW cm^{-2}). Samples were held under a vacuum.

as manifested by an absorbance increase around 550 nm and shorter wavelengths.[19,20,34,35] In these experiments, preloaded trimethylamine was used as an electron donor. The spectral changes indicate electron transfer from Zr centers to Cu, resulting in the reduction of Cu^{II} to Cu^I. No absorbance loss at 800 nm and hence no reduction of Cu^{II} was observed when the photodeposition process was attempted with single metal (Zr or Co) SBA-15 or with bare SBA-15 (Figure S1). Hence, the results demonstrate that the reduction of Cu^{II} is driven by light absorbed by the ZrOCo^{II} chromophore, which extends from the UV into the visible spectral region with an onset around 550 nm.[23] Photoconversion of Cu^{II} to Cu^I was also achieved when exciting the TiOCo MMCT absorption at 458 nm (190 mW cm^{-2}) in the presence of anchored Cu^{II}, as shown in Figure 3b. Growth of infrared bands of free, physisorbed acetonitrile at 2942, 2265, 1443, 1400, and 1375 cm^{-1} in the experiments with ZrOCo and TiOCo (Figure S2a and b, respectively) signals detachment of CH$_3$CN ligands from Cu centers during the photodeposition process, although some residual CH$_3$CN remains coordinated as indicated by the bands at 2318 and 2292 cm^{-1}.

The Cu^{II}→ Cu^I oxidation state conversion upon photodeposition was further confirmed by UV−Raman spectroscopy. The broad absorption band of the symmetric CuOCu mode with a maximum at 484 cm^{-1} observed for ZrOCo^{II} SBA-15 after loading and air oxidation of the Cu precursor complex (Figure S3a, trace 1, black) agrees exactly with the UV-Raman spectrum of a powder of CuO shown in Figure S3b, trace 3,

black. Illumination of the ZrOCo^{II} SBA-15 sample at 355 nm for 1 h results in a red shift of the band by about 5 cm^{-1} (Figure S3a, trace 2, red). The shift is close to the one measured for Cu$_2$O powder shown in Figures S3b, trace 4 (red), consistent with the reduction of a substantial fraction of Cu^{II} centers to Cu^I.

Following the photodeposition process, mild calcination at 350 °C for 5 h under air flow resulted in the formation of Cu$_x$O$_y$ clusters as shown by the analysis of high angle annular dark field (HAADF) images recorded in the scanning transmission electron microscopy (STEM) mode and energy dispersive X-ray (EDX) measurements. The results are presented in Figure 4 for ZrOCo^{II}SBA-15 and Figure S4 for
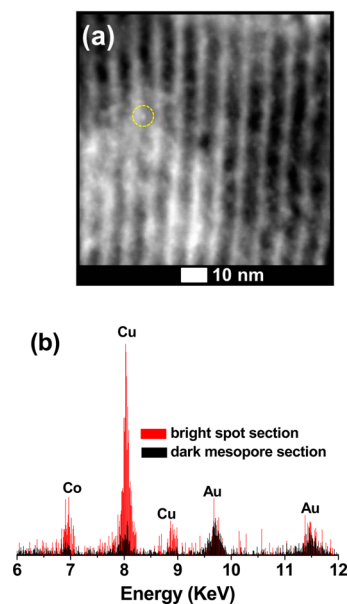

Figure 4. (a) High angle annular dark field (HAADF) images of Cu$_x$O$_y$-ZrOCo^{II} SBA-15 and (b) EDX spectra of Cu bright spot and dark mesopore section of image a. Au signals are due to the use of a gold grid.

TiOCo^{II}SBA-15. FT-IR spectra confirmed that no acetonitrile or triethylamine donor remained in the SBA-15 after calcination. The small bright spots (example marked by dotted circle) are copper oxide nanoclusters based on EDX spot analysis of five different bright spots. The EDX signal for dark areas of the mesoporous channels between the bright spots in the HAADF image of Figure 4 (Figure S4) was close to the noise level, which confirmed the assignment of the bright spots to Cu containing clusters. Histogram analysis using a digital micrograph (Gatan Microscopy Suite) program revealed an average Cu$_x$O$_y$ cluster size of 3.0 ± 0.4 nm (Figure S5).

3.2. Photochemical Reduction of Cu$_x$O$_y$ Clusters. The electronic structure (oxidation state) of the Cu centers at the Cu oxide nanocluster surface is critical for the reduction activity and possibly the selectivity of the CO$_2$ multielectron catalyst. X-ray photoelectron (XPS) and X-ray Absorption Near Edge Structure (XANES) spectroscopy are typically the preferred methods for determining oxidation states of metal containing catalysts, with XPS exhibiting surface sensitivity.[36,37] However, these methods do not allow selective probing of the oxidation state of metal centers in the top surface layer of the cluster directly exposed to the reactants. Here, infrared spectroscopy of adsorbed CO molecules provides the desired surface selectivity.

To unambiguously identify gas adsorbed carbon monoxide molecules, isotopically labeled ^{13}CO was used for these experiments.

As shown in Figure 5, spectra of adsorbed carbon monoxide are drastically different for Cu oxide nanoclusters of Cu_xO_y-
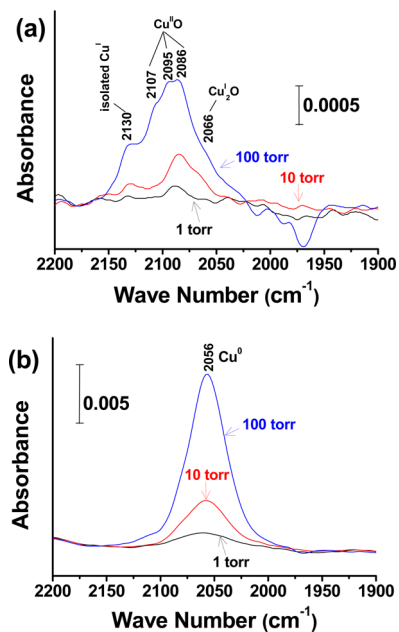

Figure 5. FT-IR spectra for ^{13}CO adsorbed on Cu_xO_y-ZrOCo SBA-15. (a) Adsorption of 1, 10, 100 Torr ^{13}CO onto the calcined clusters before photoreduction. (b) Adsorption of ^{13}CO after photoreduction at 355 nm (100 mW cm^{-2}) for 3 h. The SBA-15 wafer was 5 mg with 3.4 wt % Cu loading.

ZrOCo SBA-15 after calcination (Figure 5a) and following photoreduction at 355 nm (100 mW cm^{-2}) for 3 h using DEA (0.1 Torr) as an electron donor (Figure 5b). For the calcined clusters, the adsorbed ^{13}CO profile observed upon loading of 100 Torr gas is, as expected, dominated by Cu^{II} surface sites (2086, 2095, and 2107 cm^{-1}).[38,39] A weak shoulder at 2066 cm^{-1},[39,40] most clearly seen in Figure 5a at 10 Torr loading, indicates the presence of Cu^I centers on the clusters' surface as well as some isolated Cu^I centers on the silica nanopore surface by a shoulder at 2130 cm^{-1}.[38,41] In light of the several-fold larger extinction coefficient of the infrared band of CO adsorbed on Cu^I compared to Cu^{II},[38,42,43] the spectrum before photoreduction confirms the dominance of Cu^{II} on the nanocluster surface. After 355 nm illumination, fully reduced Cu^0 is the only detectable surface site as shown by the characteristic CO band at 2056 cm^{-1} [39,43] (Figure 5b), indicating efficient photoreduction of the cluster by the ZrOCo charge-transfer chromophore.

Photochemical reduction of the Cu_xO_y clusters coupled to TiOCo units was conducted at two wavelengths, 355 and 458 nm, in order to explore the photon energy dependence of the process. According to Figures 6a and 7a, the occupancy of CO adsorbed on the various Cu sites of Cu_xO_y-TiOCo SBA-15 after calcination very closely resembles that of Cu_xO_y-ZrOCo SBA-15 samples. By contrast, the photoreduced catalyst prepared by illumination of the TiOCo unit shows very different Cu oxidation state distributions. For 355 nm irradiation (100 mW cm^{-2}, 3 h, DEA as electron donor), a broad band with a
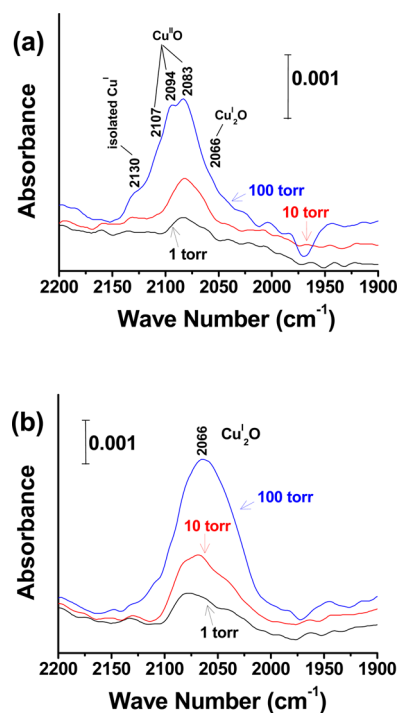

Figure 6. FT-IR spectra for ^{13}CO adsorbed on Cu_xO_y-TiOCo SBA-15. (a) Adsorption of 1, 10, 100 Torr onto the calcined clusters before photoreduction. (b) Adsorption of ^{13}CO after photoreduction at 355 nm (100 mW cm^{-2}) for 3 h. The SBA-15 wafer was 5 mg with 3.4 wt % Cu loading.
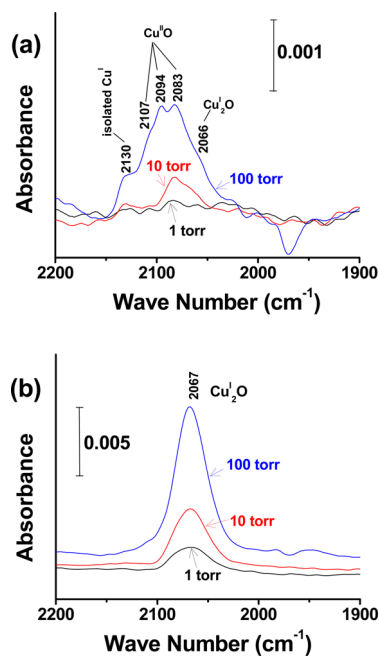

Figure 7. FT-IR spectra for ^{13}CO adsorbed on Cu_xO_y-TiOCo SBA-15. (a) Adsorption of 1, 10, 100 Torr onto the calcined clusters before photoreduction. (b) Adsorption of ^{13}CO after photoreduction at 458 nm (190 mW cm^{-2}) for 5 h. The SBA-15 wafer was 5 mg with 3.4 wt % Cu loading.

maximum at 2066 cm^{-1} observed upon 100 Torr ^{13}CO loading indicates that Cu^I centers dominate the surface layer of the catalyst. At lower loadings of 1 and 10 Torr, the adsorbed ^{13}CO band profile is clearly asymmetric with a sizable component on

the low frequency side. According to spectral deconvolution shown in Figure S6, at 1 Torr loading (Figure S6a), Cu^{II} and Cu^0 centers are the dominant adsorption sites on the Cu_xO_y cluster surface, taking into account that the extinction coefficient of CO on Cu^I is larger than that for Cu^{II} or Cu^0. IAn increase of the loading to 10 Torr results in continued adsorption on Cu^I and Cu^0 sites, while no further adsorption is observed for the Cu^{II} sites, presumably because the latter are already saturated at 1 Torr loading. An increase of the carbon monoxide pressure to 100 Torr results in exclusive additional adsorption on surface Cu^I sites (Figure S6c). Therefore, the dominant Cu sites on the cluster surface are Cu^I, with significantly smaller reservoirs of Cu^{II} and Cu^0 centers. On the other hand, when conducting the photoreduction of Cu_xO_y-TiOCo SBA-15 at longer wavelengths (458 nm, 190 mW cm^{-2}, 5 h), Cu^I are the only surface sites observed at all CO loading levels, as shown in Figure 7b. We conclude that comparison with the 355 nm result reveals a significant wavelength dependence of the photoreduction process, with the more reduced Cu^0 surface centers only formed at the higher photon energy.

While infrared bands of adsorbed CO afford assessment of the oxidation states of Cu centers at the surface, UV−vis spectra confirm photoreduction across the bulk of the Cu oxide cluster by decrease of the 800 nm Cu^{2+} (d−d) and the 350 nm charge-transfer band[35] under concurrent growth of the visible Cu_2O absorption with the onset at 630 nm (Figure S6).[34]

3.3. Photochemical Reduction of CO_2. To demonstrate carbon dioxide reduction at the Cu_xO_y cluster driven by the photoexcited $ZrOCo^{II}$ MMCT chromophore, and to investigate the influence of the surface oxidation state of the copper oxide on the photocatalysis, CO_2 reduction at Cu_xO_y-$ZrOCo^{II}$ units in SBA-15 was conducted using samples that were, or were not, photoreduced prior to CO_2 photocatalysis. As shown in Figure 8, trace 1, for the case of Cu_xO_y-$ZrOCo^{II}$SBA-15 samples that
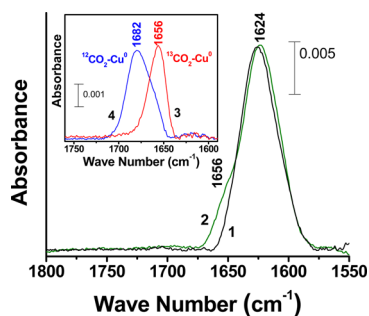

Figure 8. FT-IR spectra for $^{13}CO_2$ adsorbed on calcined Cu_xO_y-ZrOCo SBA-15 (trace 1, black) and reduced Cu_xO_y-ZrOCo SBA-15 (trace 2, green). Inset, trace 3, red: Difference spectrum (2 − 1), which shows the infrared band of $^{13}CO_2$ adsorbed on the Cu^0 surface. Trace 4, blue: Corresponding difference spectrum of $^{12}CO_2$ adsorbed on Cu^0. The SBA-15 wafer was 5 mg with 3.4 wt % Cu loading.

were not subject to photoreduction after calcination, a broad absorption at 1624 cm^{-1} upon loading of 760 Torr $^{13}CO_2$ and 0.5 Torr DEA indicates formation of the familiar carboxylate type structure of weakly adsorbed carbon dioxide on metal oxide surfaces.[44−46] By contrast, loading of Cu_xO_y-ZrO-Co^{II}SBA-15 material with $^{13}CO_2$ that was first photoreduced gave an additional infrared band at 1656 cm^{-1}, as shown in Figure 8, trace 2. The corresponding band in the case of $^{12}CO_2$ loading was at 1682 cm^{-1} (inset of Figure 8). We attribute the

new band to carbon dioxide molecules adsorbed on Cu^0 surface sites featuring a carboxylate structure, consistent with infrared spectra of CO_2 adsorbed on metallic Cu surfaces.[47]

Illumination at 355 nm (100 mW cm^2) resulted in consumption of the adsorbed carbon dioxide species for the Cu_xO_y-$ZrOCo^{II}$SBA-15 sample that was subject to prior photoreduction. Figure 9 shows the depletion of the 1682
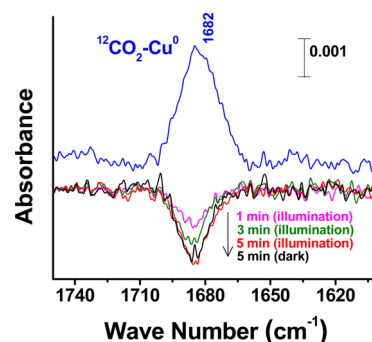

Figure 9. FT-IR spectra of $^{12}CO_2$ adsorbed on reduced Cu_xO_y-ZrOCo SBA-15 after carbon dioxide loading (760 Torr) and subsequent evacuation (blue trace). Additional spectral traces show depletion of the band upon 355 nm irradiation (100 mW cm^{-2}) for 1 min (pink), 3 min (green), and 5 min (red) in the presence of 0.5 Torr diethylamine donor. The black trace was recorded after a subsequent dark period of 5 min. No replenishment is observed in the dark period because CO_2 was removed by evacuation. The SBA-15 wafer was 5 mg with 3.4 wt % Cu loading.

cm^{-1} $^{12}CO_2$ species during the first few minutes of photolysis (the experiment with $^{12}CO_2$ is shown here because there is less overlap with the residual H_2O band at 1635 cm^{-1} than in the case of $^{13}CO_2$). In prolonged photolysis experiments in the presence of 760 Torr CO_2, the adsorbed 1682 cm^{-1} species is continually replenished, which results in a steady state concentration of the surface species. Illumination at 355 nm (100 mW cm^{-2}) of a sample that was subject to prior photoreduction resulted in the formation of carbon monoxide as indicated by the absorbance growth of the ro-vibrational bands of gas phase ^{13}CO in the region 2075 to 2050 cm^{-1} over a period of 5 h (Figure 10a). The growth kinetics of the ^{13}CO product shown in trace 1 (red) of Figure 10b is close to linear with time, with 59.2 nmol CO produced over the 5 h photolysis period. To minimize the systematic error of intensity measurements caused by the smaller natural line width of CO ro-vibrational bands (0.01 cm^{-1}) compared to the resolution of the spectrometer (0.25 cm^{-1}), integrated intensities were used. The growth is about 3 times faster than an otherwise identical CO_2 reduction experiment with a Cu_xO_y-$ZrOCo^{II}$SBA-15 sample that was not subject to prior photoreduction treatment (Figure 10b, trace 2 (black)).The rate of CO_2 reduction upon continued photocatalysis using this sample will eventually approach that of the prereduced Cu_xO_y-ZrOCo as surface Cu centers are gradually reduced to the Cu^0 state. For illumination at 458 nm (190 mW cm^{-2}) of the Cu_xO_y-$TiOCo^{II}$ unit that was photoreduced prior to $^{13}CO_2$ reduction, ^{13}CO production was 10 times lower than for clusters driven by the $ZrOCo^{II}$ chromophore (Figure 10b, trace 3 (blue)). No CO_2 photoreduction was observed under identical illumination conditions for Cu_xO_ySBA-15 samples which have no ZrOCo units (Figure 10b, trace 4 (green)), demonstrating that direct light absorption by the cuprous oxide
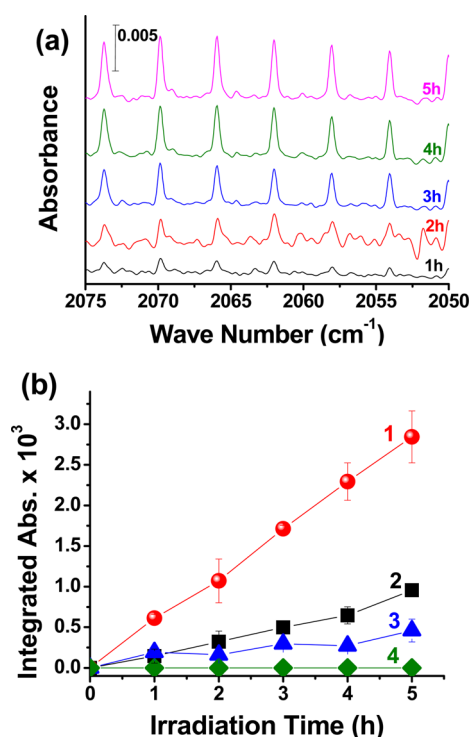
Figure 10. (a) Difference FT-IR spectrum (2075−2055 cm⁻¹) of gas phase ^{13}CO growth upon 355 nm irradiation (100 mW cm⁻²) of Cu_xO_y-ZrOCo^{II}SBA-15 (5 mg pellet, 3.4 wt % Cu_xO_y) for 1 h (black), 2 h (red), 3 h (blue), 4 h (green), and 5 h (pink) in the presence of 760 Torr $^{13}CO_2$ and 0.5 Torr diethylamine. The sample was photoreduced prior to loading of carbon dioxide. (b) Growth kinetics of ^{13}CO (at 2065.9 cm⁻¹ band) on Cu_xO_y-ZrOCo^{II}SBA-15 upon 355 nm irradiation (100 mW cm⁻²) with (trace 1, red) and without (trace 2, black) photoreduction of the sample prior to carbon dioxide loading. Trace 3 (blue) shows ^{13}CO growth in a Cu_xO_y-TiOCo^{II}-SBA-15 sample upon 458 nm irradiation (190 mW cm⁻²) that was photoreduced prior to carbon dioxide loading. No ^{13}CO was produced in the case of the Cu_xO_y(no photodeposition)-SBA-15 sample (trace 4, green) without ZrOCo sites present.

cluster does not contribute to the observed photocatalysis on a time scale under which the Cu_xO_y-ZrOCo^{II} system readily shows CO production.

In addition to gas phase carbon monoxide, adsorbed ^{13}CO with a maximum at 2056 cm⁻¹ was also formed, as can be seen in Figure 11. Hence, the photoproduct adsorbed primarily on the Cu^0 site, which is the main surface site of prereduced Cu_xO_y. The spectra were recorded at a lower resolution of 1 cm⁻¹ in order to show more clearly the contribution of the broad bands of adsorbed ^{13}CO. For clarity, minor contributions of ^{12}CO generated by concurrent photodecomposition of the electron donor DEA were removed by spectral subtraction, shown in Figure S9.

4. DISCUSSION

The observation of photoreduction of surface Cu centers from oxidation state Cu^{II} to Cu^0 or Cu^I upon excitation of the Zr^{IV}OCo^{II} → Zr^{III}OCo^{III} MMCT transition demonstrates the functional Cu_xO_y-ZrOCo unit in which the transiently reduced Zr acceptor transfers electrons to the nanocluster catalyst. Hence, the photodeposition method introduced in this work provides the proper coupling of the acceptor metal center with the catalyst cluster. While the precise atomic structure of the
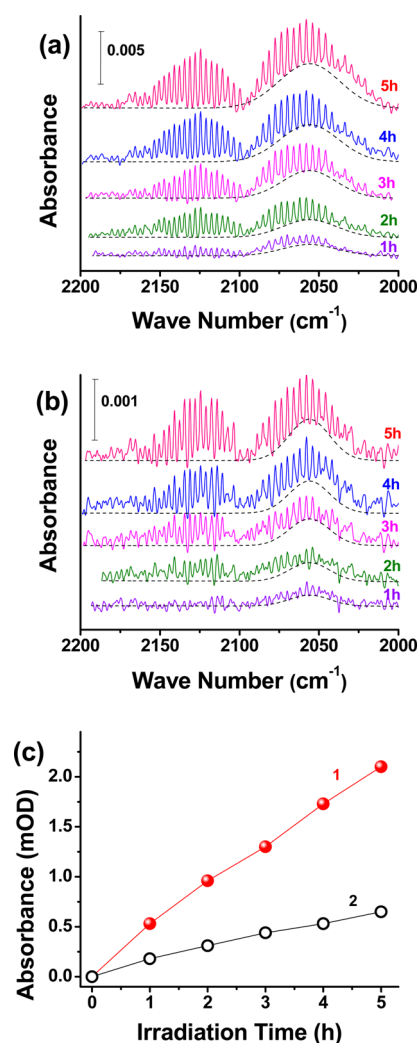
Figure 11. Difference FT-IR spectrum (2200−2000 cm⁻¹) of gas phase and adsorbed ^{13}CO growth upon 355 nm irradiation (100 mW cm⁻²) of Cu_xO_y-ZrOCo^{II}SBA-15 with (a) and without (b) photoreduction of the sample prior to carbon dioxide loading (5 mg pellet, 3.4 wt % Cu_xO_y) for 1 h (violet), 2 h (green), 3 h (pink), 4 h (blue), and 5 h (red) in the presence of 760 Torr $^{13}CO_2$ and 0.5 Torr diethylamine. (c) Growth kinetics of ^{13}CO adsorbed (at 2056 cm⁻¹ band) on Cu_xO_y-ZrOCo^{II}SBA-15 with (trace 1, red) and without (trace 2, black) photoreduction of the sample prior to carbon dioxide loading.

coupled Zr acceptor center and Cu oxide cluster is not revealed by the current vibrational and optical spectroscopy measurements, the observed strong dependence of the CO_2 photoreduction yield on the oxidation state of the surface Cu centers directly proves that CO_2 is reduced on the Cu_xO_y surface. As expected, no CO_2 reduction is observed at Cu_xO_y clusters if the ZrOCo chromophore is absent. Furthermore, the CO_2 reduction yields depend strongly on the chemical identity of the acceptor (Zr versus Ti) and the photolysis wavelength used for MMCT excitation. Hence, these photochemical observations establish that the heterobinuclear unit functions as a light absorber, donating electrons to the Cu_xO_y catalyst on whose surface CO_2 is reduced.

Among the studies of metallic Cu nanoparticles and Cu oxide nanoclusters for photo or electrocatalytic reduction of CO_2 reported in the literature,[6−8] the work reported here constitutes one of just a few examples in which the oxidation state of

surface Cu centers is spectroscopically defined and the relationship to catalytic activity or selectivity investigated. Using Cu L-edge XANES and Auger spectroscopy, Le et al. identified Cu^I centers as active sites for electrochemical reduction of CO_2 to methanol.[12] Li and Kanan established that Cu^0 and Cu^I at the surface of an electrocatalyst prepared by two step oxidation/reduction of Cu foil, which were identified by XPS, showed better selectivity to CO and HCOOH than in the absence of the pretreatment.[9] The coexistence of Cu^I and metallic Cu was also found beneficial for the selective electrocatalytic reduction of CO_2 by Garcia-Esparza et al. using the surface sensitive XPS technique to probe the Cu oxidation state.[48] Hence, our finding that reduced Cu centers on the Cu_xO_y nanocluster surface are substantially more active toward CO_2 reduction is mirrored by the results of these electrocatalytic studies. The advantage of monitoring the oxidation state of Cu on the catalyst surface by infrared spectroscopy of adsorbed CO molecules is the noninvasiveness of the method compared to probing with X-rays under high vacuum conditions.

The dominant role of Cu^I centers for CO_2 reduction to methanol was also noticed in UV photochemical studies of Cu_2O cocatalyst attached to TiO_2 nanoparticles (2 wt % Cu) based on XPS and X-ray spectroscopic characterization.[17,49−51] Further studies indicate that the size and morphology of the Cu_2O catalyst nanoparticles on TiO_2 influence product selectivity, in addition to the specific reaction conditions. For example, Cu_2O functionalized TiO_2 particles at very light loading (0.04 wt % Cu) illuminated at lower photon energy gave methane as a major product instead.[52] Cu_2O crystalline particles as stand-alone visible light absorbing catalysts have been found to exhibit facet selectivity in aqueous media with respect to competing hydrogen generation.[53] CuO nanoparticles on TiO_2, on the other hand, play a different mechanistic role in photodriven CO_2 reduction, namely as a p-type semiconductor component forming a p−n heterojunction in the CuO/TiO_2 particle.[54,55] Detailed knowledge of the electronic structure provided by spectroscopy is essential for guiding the preparation of Cu based nanoparticle catalysts for CO_2 reduction.

5. CONCLUSIONS

The all-inorganic system for the CO_2 reduction half reaction consisting of a heterobinuclear light absorber coupled to a cuprous oxide nanocluster introduced here points to the general utility of metal-to-metal charge-transfer excitation as a method for achieving proper hierarchical arrangement of the photocatalytic assembly. The ability to manipulate the oxidation state of surface Cu centers, with Cu^0 giving the highest photoreduction rates provides direct evidence for the cuprous oxide cluster acting as multielectron catalyst driven by the ZrOCo charge transfer unit. Successful coupling of the binuclear unit with the catalyst nanocluster is further manifested by the strong dependence of the CO_2 reduction rate on the nature of the acceptor center (Zr versus Ti) and the photolysis excitation wavelength used. Time-resolved FT-IR experiments are currently in progress for elucidating the detailed mechanism for CO_2 reduction on the cuprous oxide catalyst surface. Detection and structural identification of intermediates is expected to provide insights for steering the catalysis to deeper reduction products beyond CO.

AUTHOR INFORMATION

Corresponding Author
*Phone: (510) 486 4325. E-mail: HMFrei@lbl.gov.

Notes
The authors declare no competing financial interest.

REFERENCES

(1) Koike, K.; Naito, S.; Sato, S.; Tamaki, Y.; Ishitani, O. *J. Photochem. Photobiol., A* **2009**, *207*, 109−114.
(2) Bian, Z. Y.; Chi, S. M.; Li, L.; Fu, W. *Dalton Trans.* **2010**, *39*, 7884−7887.
(3) Schneider, J.; Vuong, K. Q.; Calladine, J. A.; Sun, X. Z.; Whitwood, A. C.; George, M. W.; Perutz, R. N. *Inorg. Chem.* **2011**, *50*, 11877−11889.
(4) Kiyosawa, K.; Shiraishi, N.; Shimada, T.; Masui, D.; Tachibana, H.; Takagi, S.; Ishitani, O.; Tryk, D. A.; Inoue, H. *J. Phys. Chem. C* **2009**, *113*, 11667−11673.
(5) Kim, W.; Yuan, G.; McClure, B. A.; Frei, H. *J. Am. Chem. Soc.* **2014**, *136*, 11034−11042 and references therein..
(6) Hori, Y. In *Modern Aspects of Electrochemistry*; Springer, New York, 2008; Vol. *42*, pp 89−189.
(7) Gattrell, M.; Gupta, N.; Co, A. *J. Electroanal. Chem.* **2006**, *594*, 1−19.
(8) Schouten, K. J. P.; Kwon, Y.; van der Ham, C. J. M.; Qin, Z.; Koper, M. T. M. *Chem. Sci.* **2011**, *2*, 1902−1909.
(9) Li, C. W.; Kanan, M. W. *J. Am. Chem. Soc.* **2012**, *134*, 7231−7234.
(10) Reske, R.; Mistry, H.; Behafarid, F.; Roldan Cuenya, B.; Strasser, P. *J. Am. Chem. Soc.* **2014**, *136*, 6978−6986.
(11) Varela, A. S.; Schlaup, C.; Jovanov, Z. P.; Malacrida, P.; Horch, S.; Stephens, I. E. L.; Chorkendorff, I. *J. Phys. Chem. C* **2013**, *117*, 20500−20508.
(12) Le, M.; Ren, M.; Zhang, Z.; Sprunger, P. T.; Kurtz, R. L.; Flake, J. C. *J. Electrochem. Soc.* **2011**, *158*, E45−E49.
(13) Sen, S.; Liu, D.; Palmore, G. T. R. *ACS Catal.* **2014**, *4*, 3091−3095.
(14) Reske, R.; Duca, M.; Oezaslan, M.; Schouten, K. J. P.; Koper, M. T. M.; Strasser, P. *J. Phys. Chem. Lett.* **2013**, *4*, 2410−2413.
(15) Kim, D.; Resasco, J.; Yu, Y.; Asirl, A. M.; Yang, P. *Nat. Commun.* **2014**, *5*, 4948.
(16) Rasul, S.; Anjum, D. H.; Jedidi, A.; Minenkov, Y.; Cavallo, L.; Takanabe, K. *Angew. Chem., Int. Ed.* **2015**, *54*, 2146−2150.
(17) Tseng, I. H.; Wu, J. C. S. *Catal. Today* **2004**, *97*, 113−119.
(18) Tennakone, K.; Jayatissa, A. H.; Punchihewa, S. *J. Photochem. Photobiol., A* **1989**, *49*, 369−375.
(19) Lin, W.; Frei, H. *J. Am. Chem. Soc.* **2005**, *127*, 1610−1611.
(20) Lin, W.; Frei, H. *J. Phys. Chem. B* **2005**, *109*, 4929−4935.

(21) Han, H.; Frei, H. *Microporous Mesoporous Mater.* **2007**, *103*, 265−272.

(22) Han, H.; Frei, H. *J. Phys. Chem. C* **2008**, *112*, 8391−8399.

(23) Macnaughtan, M. L.; Frei, H.; Soo, H. S. *J. Phys. Chem. C* **2014**, *118*, 7874−7885.

(24) McClure, B. A.; Frei, H. *J. Phys. Chem. C* **2014**, *118*, 11601−11611.

(25) Maschmeyer, T.; Rey, F.; Sankar, G.; Thomas, J. M. *Nature* **1995**, *378*, 159−162.

(26) Kang, K. K.; Ahn, W. S. *J. Mol. Catal. A: Chem.* **2000**, *159*, 403−410.

(27) Bouh, A. O.; Rice, G. L.; Scott, S. L. *J. Am. Chem. Soc.* **1999**, *121*, 7201−7210.

(28) Nakamura, R.; Frei, H. *J. Am. Chem. Soc.* **2006**, *128*, 10668−10669.

(29) Han, H.; Frei, H. *J. Phys. Chem. C* **2008**, *112*, 16156−16159.

(30) Manch, W.; Fernelius, W. C. *J. Chem. Educ.* **1961**, *38*, 192−201.

(31) Hathaway, B. J.; Holah, D. G.; Underhill, A. E. *J. Chem. Soc.* **1962**, 2444−2448.

(32) Weiner, H.; Hayashi, Y.; Finke, R. G. *Inorg. Chem.* **1999**, *38*, 2579−2591.

(33) Lever, A. B. P. *Inorganic Electronic Spectroscopy*, 2nd ed.; Elsevier: Amsterdam, 1984; p 355.

(34) Texter, J.; Strome, D. H.; Herman, R. G.; Klier, K. *J. Phys. Chem.* **1977**, *81*, 333−338.

(35) Zhu, Z. H.; Zhu, H. Y.; Wang, S. B.; Lu, G. Q. *Catal. Lett.* **2003**, *91*, 73−81.

(36) Irie, H.; Kamiya, K.; Shibanuma, T.; Miura, S.; Tryk, D. A.; Yokoyama, T.; Hashimoto, K. *J. Phys. Chem. C* **2009**, *113*, 10761−10766.

(37) Liu, L.; Zhao, C.; Li, Y. *J. Phys. Chem. C* **2012**, *116*, 7904−7912.

(38) Kohler, M. A.; Cant, N. W.; Wainwright, M. S.; Trimm, D. L. *J. Catal.* **1989**, *117*, 188−201.

(39) Hollins, P. *Surf. Sci. Rep.* **1992**, *16*, 51−94.

(40) Yang, C. C.; Yu, Y. H.; van der Linden, B.; Wu, J. C. S.; Mul, G. *J. Am. Chem. Soc.* **2010**, *132*, 8398−8406.

(41) Hadjiivanov, K. I.; Kantcheva, M. M.; Klissurski, D. G. *J. Chem. Soc., Faraday Trans.* **1996**, *92*, 4595−4600.

(42) Schneider, W. F.; Hass, K. C.; Ramprasad, R.; Adams, J. B. *J. Phys. Chem.* **1996**, *100*, 6032−6046.

(43) Coloma, F.; Marquez, F.; Rochester, C. H.; Anderson, A. *Phys. Chem. Chem. Phys.* **2000**, *2*, 5320−5327.

(44) Ulagappan, N.; Frei, H. *J. Phys. Chem. A* **2000**, *104*, 7834−7839.

(45) Baltrusaitis, J.; Schuttlefield, J.; Zeitler, E.; Grassian, V. H. *Chem. Eng. J.* **2011**, *170*, 471−481.

(46) Busca, G.; Lorenzelli, V. *Mater. Chem.* **1982**, *7*, 89−126.

(47) Knurr, B. J.; Weber, J. M. *J. Phys. Chem. A* **2014**, *118*, 10246−10251.

(48) Garcia-Esparza, A.; Limkrailassiri, K.; Leroy, F.; Rasul, S.; Yu, W.; Lin, L.; Takanabe, K. *J. Mater. Chem. A* **2014**, *2*, 7389−7401.

(49) Tseng, I.-H.; Chang, W.-C.; Wu, J. C. S. *Appl. Catal., B* **2002**, *37*, 37−48.

(50) Tseng, I.-H.; Wu, J. C. S.; Chou, H.-Y. *J. Catal.* **2004**, *221*, 432−440.

(51) Wu, J. C. S.; Lin, H.-M.; Lai, C.-L. *Appl. Catal., A* **2005**, *296*, 194−200.

(52) Liu, D.; Fernandez, Y.; Ola, O.; Mackintosh, S.; Maroto-Valer, M.; Parlett, C. M. A.; Lee, A. F.; Wu, J. C. S. *Catal. Commun.* **2012**, *25*, 78−82.

(53) Handoko, A. D.; Tang, J. *Int. J. Hydrogen Energy* **2013**, *38*, 13017−13022.

(54) In, S.-I.; Vaughn, D. D., II; Schaak, R. E. *Angew. Chem., Int. Ed.* **2012**, *51*, 3915−3918.

(55) Qin, S.; Xin, F.; Liu, Y.; Yin, X.; Ma, W. *J. Colloid Interface Sci.* **2011**, *356*, 257−261.